
PHYSICS PERCEPTION IN SLOSHING SCENES WITH GUARANTEED THERMODYNAMIC CONSISTENCY

A PREPRINT

Beatriz Moya

Aragon Institute in Engineering Research
 University of Zaragoza
 Zaragoza, Spain
 beam@unizar.es

Alberto Badias

Aragon Institute in Engineering Research
 University of Zaragoza
 Zaragoza, Spain
 abadias@unizar.es

David Gonzalez

Aragon Institute in Engineering Research
 University of Zaragoza
 Zaragoza, Spain
 gonzal@unizar.es

Francisco Chinesta

ESI Group chair. PIMM Lab.
 ENSAM Institute of Technology
 Paris, France
 francisco.chinesta@ensam.eu

Elias Cueto

Aragon Institute in Engineering Research
 University of Zaragoza
 Zaragoza, Spain
 ecueto@unizar.es

June 28, 2021

ABSTRACT

Physics perception very often faces the problem that only limited data or partial measurements on the scene are available. In this work, we propose a strategy to learn the full state of sloshing liquids from measurements of the free surface. Our approach is based on recurrent neural networks (RNN) that project the limited information available to a reduced-order manifold so as to not only reconstruct the unknown information, but also to be capable of performing fluid reasoning about future scenarios in real time. To obtain physically consistent predictions, we train deep neural networks on the reduced-order manifold that, through the employ of inductive biases, ensure the fulfillment of the principles of thermodynamics. RNNs learn from history the required hidden information to correlate the limited information with the latent space where the simulation occurs. Finally, a decoder returns data back to the high-dimensional manifold, so as to provide the user with insightful information in the form of augmented reality. This algorithm is connected to a computer vision system to test the performance of the proposed methodology with real information, resulting in a system capable of understanding and predicting future states of the observed fluid in real-time.

Keywords Physics perception · thermodynamics-aware deep learning · GENERIC · sloshing

1 Introduction

World simulation recreates the response of an environment where a robot operates [1]. For AI-enabled robotics, these systems are crucial for emulating their sensing and understanding capacities and perform the mission they have been entrusted. Fluid manipulation is a rather difficult task to be accomplished and trustable physics-based simulation of liquids is desired for success [2] [3] [4].

The merge of knowledge-driven and data-driven learning is settling in these areas, enabling the study of complex systems of highly non-linear nature [5]. This is known generally under the name of “physics-informed deep learning”, although very different techniques may fall under this broad classification. In spite of the common interest in introducing well-known physical knowledge into these approaches, there is a great divergence of proposals to be considered. From solving PDEs [6] [7] to learning constitutive laws based on invariants and conserved quantities [8] [9], these works establish a strong framework to work towards generalizable deep learning.

These techniques keep expanding but access to the full set of experimental variables explaining the state of the fluid is not always available. In addition, information comes usually from cameras in the form of video streams. This means that some 30 to 120 frames per second will be available, and a similar feedback rate is expected for the system so as to transmit a smooth sensation to the user. Under such stringent rates, encoding the information available to a low-dimensional manifold where we can leverage the underlying features of data to predict the unseen information is mandatory. Such a framework would help to unveil internal variables from partial measurements that we may need in the physics-aware descriptions proposed. By these means, we establish a bridge between real systems with their digital twins [10] [11].

The aim of the present work is to develop a system for fluid dynamics understanding and reasoning by means of data-driven modeling and simulation whose result is thermodynamically admissible. The simulation engine is of course coupled with a computer vision system to build online digital twins of fluids. The performance of the loop must achieve real-time speed to guarantee a trustable decision making.

In our approach, the information we require for physics-informed prediction is inaccessible to a commodity depth camera (we do not consider here more sophisticated systems such as particle image velocimetry, for instance). We hypothesize that the knowledge of the internal variables we need for a complete description of the fluid will come, on one hand, from the training with full-field pseudo-experimental data coming from simulations and, on the other, from the history of partial measurements performed during runtime. Therefore, during runtime we use recurrent neural networks (RNNs) to partially alleviate the lack of information that we need to complete the simulation. The RNN reconstructs the information to perform adequate simulations. Also, it projects the state of the fluid to a reduced-order space where simulations are performed to achieve real-time performance.

To guarantee the thermodynamic admissibility of the resulting simulations, we actually learn from data a particular formulation of the dynamics based on the so-called General Equation for the Non-Equilibrium Reversible-Irreversible Coupling (GENERIC) formalism [12]. GENERIC constitutes a generalization of Hamiltonian dynamics to dissipative phenomena. Under the scope of GENERIC acting as an inductive bias during the learning procedure, we ensure the accomplishment of the basic principles of energy conservation and entropy generation, thus providing a physically sound learning framework.

The paper is structured as follows. Section 2 describes the state of the art with regard to recent works in the field. Section 3 describes the problem in detail. Section 4 discloses the method, from the projection of the dynamics to a lower dimensional manifold, to the physics learning and the connection with partial measurements. The training and implementation details are explained across section 5. Section 6 showcases the results obtained with real world measurements. We end up with a discussion of the results and an evaluation of the future developments that can derive from this work.

2 Works in the field

2.1 Self-supervised estimation of dynamical states

Labelling is an indisputable bottleneck for data-driven prediction. High-accuracy descriptions often require unaffordable high-dimensional datasets that inevitably drive towards the curse of dimensionality. On top of that, industries and engineering applications aim to perform surrogate design with few simulations. Thus, we need a background of understanding that substitutes the need of labeling, enabling machine self-intuition for deep understanding of the information available.

Natural language processing could be seen as one of the richest fields in terms of self-supervised learning (SSL) since this philosophy has been fully assimilated for years. Their predicting systems are prolific sources of new techniques and approaches of SSL [13] [14].

Computer vision also faces the need to work with augmented datasets from limited labeled data and storage [15] [16], and the need of recovering information [17] [18]. They propose image-based algorithms based on different approaches such as relative positioning [19], colorization [20], image transformations [21], and generative modeling for reconstruction [22] among others. SimCRL [23] outperforms at learning image representations via contrastive learning

minimizing the contrastive loss in augmented views of data samples. [24] suggests learning invariant representations from images which enable reconstruction under certain transformations.

Continuing with image-based techniques, SSL has also a clear importance in robotics and visual perception and understanding [25] [26]. Yan et al. [27] predict rope states from a neural network trained with rendered images. A self-supervised learning scheme is proposed to match real images with the rendered information with which the simulator has been trained by means of comparing segmentation masks.

In contrast with image-based methods, mechanics and dynamics typically use strategically placed sensors that acquire data to recover the full set of quantities from sparse observations [28] [29] [30]. A number of works employ deep neural networks (DNN) for this purpose. Erichson et al. [31] claim the use of shallow neural networks for reconstructing fluid flows. [32] considers a mapping from a simplified problem to a target benchmark. In this case, learning is performed over the simplified case for solving the problem, and then the solution is mapped back performing the connection between the simplified and target POD representations. Lye et al. [33] estimate the unknown input parameters in turbulent flows from observables. They employ a fully connected neural network that approximates the observable maps in a regime of low regularity.

Our contribution consists of a hybrid proposal between image- and physics-based reconstruction. Instead of employing sensors, information is extracted from the detected free surface of liquids by means of computer vision analysis. The free surface is detected and evaluated from raw video frames. The information is then projected into a latent manifold for simulation. An augmented reconstruction is provided outputting not only the state of the fluid volume, but also velocity, internal energy, and stress fields.

2.2 Deep learning incorporating physics priors

In spite of the use of self-supervised learning to compensate the lack of unlabeled data, supervised methods still need a large database for learning a model. Few data could jeopardize the accuracy of the approximations. Black-box schemes do not succeed at this task since very often not enough information is provided to learn global expressions and efficient generalizations [34]. Inductive biases [35] enforce the network to learn certain relationships on data to lead to a target function. On top of that, they contribute to reach convergence and reduce error bounds [36]. As a result, less data is required and the results are more realistic and accurate.

Raissi et al. [6] could be considered among the pioneer works in the field of physics-informed deep learning for mechanics. From this point, many approaches have leveraged theoretical knowledge to improve the learning procedure [37] [38]. Hamiltonian (thus, conservative) systems are regular test benchmarks for these techniques [39] [40]. Nevertheless, some important systems, such as those that involve Newtonian and non-Newtonian fluid dynamics, require beyond-equilibrium schemes. Thermodynamics constitute a framework that enables the study of any physical system, including those of inherent dissipative nature. Yu et al. [41] apply the generalized Onsager principle to unveil the relationships among the state variables to ensure the fulfillment of the principle for a Runge-Kutta integration scheme.

GENERIC [12] describes the evolution in time of a set of variables—that must be complete in the sense of being able to describe the energy of the system—with regard to the evolution of energy and entropy of the system under study. By learning the slow manifold of their evolution, the dynamics can be fully described at a coarse-grained scale [42]. This learning theory has been successfully applied to model rather different and complex behaviors [43] [44] [45] [46]. In recent works, it has been coupled with DNNs to build the so-called Structure Preserving Neural Networks (SPNN) [47] [48].

In the context of scene understanding and interaction with fluids, there exist plenty of approaches [49] [50] [51] [4]. We believe in the application of thermodynamic priors through the enforcement of the GENERIC formalism to discover fast and accurately relationships for such perception and interaction tasks.

3 Problem description

In this work we propose a strategy in which learned simulators are employed as the engine of physical scene understanding. Similar strategies have been developed in recent times, see [51], for instance. However, as an important difference with respect to these works, here we aim at developing a technique in which quantitative—and not only qualitative—information is key. This is of utmost importance if our perception system is to be employed in an industrial framework, in the form of a digital twin of an asset, for instance. Thus, it is of primary importance to ensure that the learned simulator is able to make predictions that adhere to known basic principles of physics, such as the laws of thermodynamics.

We have considered the problem of fluid sloshing as a proof of concept for this analysis. This is in part due to its practical interest (to construct robots able to manipulate fluids, for instance) but also for its generality: sloshing is a (nonlinear) physical phenomenon that presents several interesting and challenging characteristics. Among them, it is a dissipative phenomenon. While there is a plethora of works devoted to learning conservative phenomena, based upon Hamiltonian or Lagrangian descriptions (see, among others, [9] [52] [53] [54] [55] [56]), very little has been investigated for learning dissipative phenomena.

We consider a system whose time evolution is described in terms of a set of state variables that ensure a full description of its thermodynamical state. In general, any physical system can be described at different levels, that incorporate different amounts of information. Coarser levels incorporate less information, but also involve less degrees of freedom [57]. Thus, at the molecular dynamics scale, positions and momenta of every molecule describe completely the physics. While at this scale Newtonian laws apply and everything is conservative, the number of degrees of freedom, and also the time scale at which the phenomenon evolves, makes this type of description useless. At any other, coarser level, the effect of unresolved variables on the evolution of resolved ones introduces dissipation, by the celebrated fluctuation-dissipation theorem.

At a hydrodynamics level, position, velocity, internal energy and stress fields are the state variables required for a full description of a (possibly non-Newtonian) fluid dynamics scenario in terms of the GENERIC formalism [58]. Thus, for a fluid discretized into M particles, the set \mathcal{S} of variables will be

$$\mathcal{S} = \{z = (r_j, v_j, E_j, \tau_j, j = 1, 2, \dots, M) \in (\mathbb{R}^3 \times \mathbb{R}^3 \times \mathbb{R} \times \mathbb{R}^6)^M\}.$$

With the help of an RGBD camera, whose detailed description is carried out in Section 6.1, only partial measurements of these variables are possible. We are not interested in using complex laboratory equipments such as particle imaging velocimetry, for instance, that would greatly limit the generality of our approach. Instead, with the help of the camera we have access to the position of the free surface of the fluid at each frame, as will be detailed below. This severely limits the amount of information at our disposal, and obliges us to develop a system able to unveil hidden information. In this sense, our methodology is somehow linked to (at least, partially) self-supervised methodologies.

As a proof of concept, we implement the learning algorithm to perceive the physics of different fluids contained in a glass subjected to arbitrary movements made with our hand. This phenomenon has been first reproduced computationally for different velocities so as to obtain time-discretized pseudo-experimental data of the fluid volume, which had previously been discretized into M particles. It has been computationally modeled and simulated by employing Smooth Particle Hydrodynamics [59]. We perform four simulations per fluid by applying four different initial glass velocities to trigger the dynamics. Then, we evaluate the state of the fluid at discretized time steps for each simulation. The required state variables are evaluated and stored at each particle for each time step. As a result, we have a collection of snapshots that describe the state of the fluid to perform training of the networks. Afterwards, the system must be able to predict and interpret the behavior of a glass under different, previously unseen, conditions with limited information about its actual conditions.

4 Methodology and architecture

The complexity of the task just presented obliges us to implement our system in three different steps, that are described here. See Fig. 1 for a graphical sketch of the implemented architecture. The highly dimensional nature of the problem motivates the reduction of the dynamics to carry out learning on an embedded space of much lower dimension. In the case of learning and predicting new situations from real world data, we need to establish a correlation between the data available (position of the free surface) and the latent space built from full computational descriptions. We hypothesize with the existence of features in the data sequence that correlate these partial measurements with the history and internal variables of the fluid. An architecture based on recurrent neural networks can unveil the correlations and map the data acquired to the latent space, and output the reconstructed state in the next time step.

To accomplish these requirements, we need to develop three different architectures. Firstly, we have to project our pseudo-experimental data, with which we will train our simulator at step 1, to a lower dimensional manifold to train the algorithm efficiently and achieve real-time performance in the computation. As a second step, we work over an algorithm based on recurrent neural networks to substitute the encoder by a perceptron capable of projecting partial measurements to the latent space. Finally, we need to train a physics-informed integrator that will learn the evolution of the dynamics in the latent space.

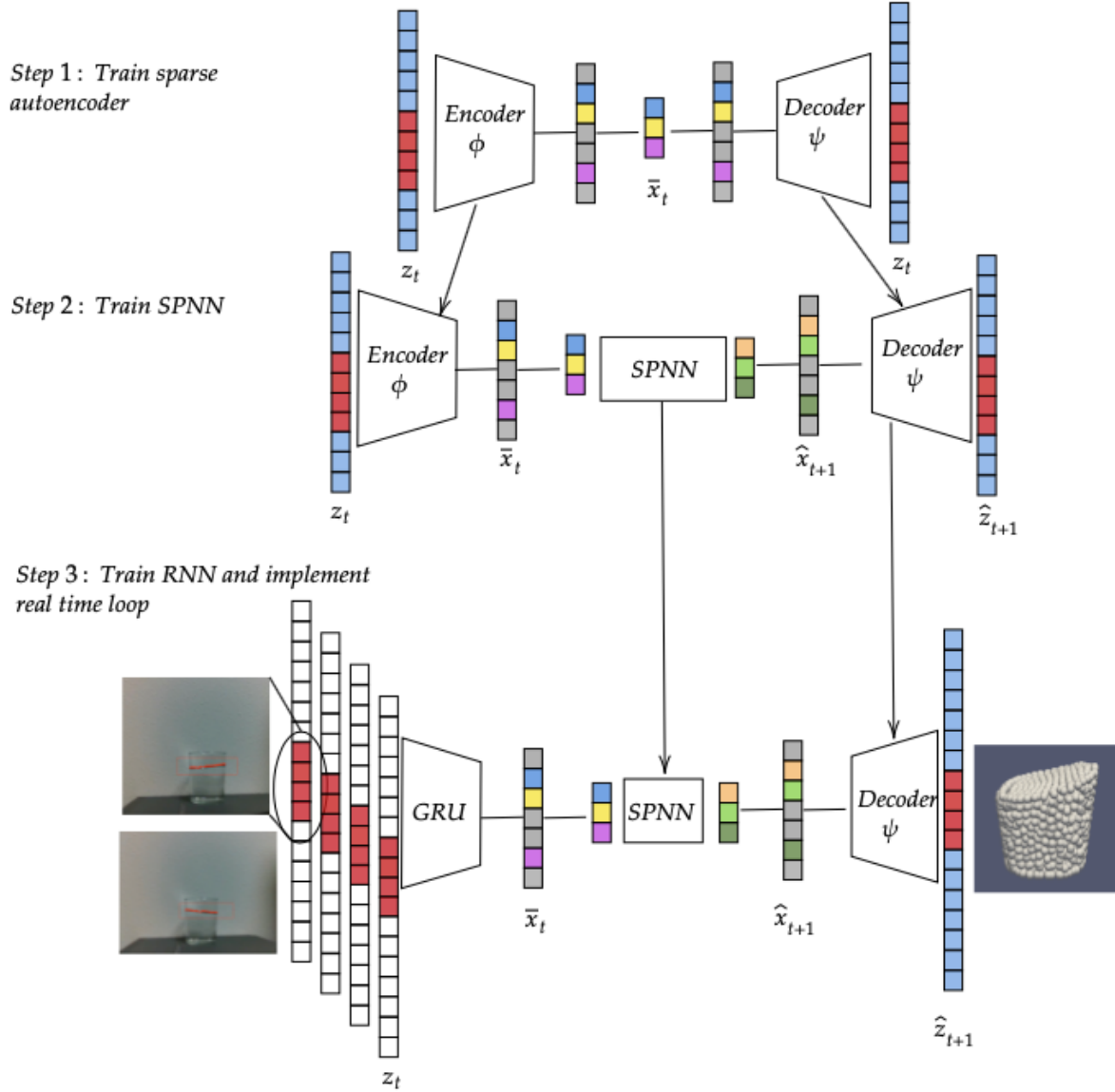


Figure 1: Sketch of the construction procedure for the deep neural network able to perceive sloshing phenomena. In a first step (first row), we must unveil the intrinsic dimensionality of the problem. To that end, we train a sparse autoencoder from pseudo-experimental full-field data. Once the number of variables governing the physics has been determined, we must train a structure-preserving neural network, able to integrate in time the state of the system. Thus, at step 2 in the figure, given the state of the system at time t , the decoder will output the state of system at time $t + \Delta t$. But the main difficulty is that during runtime we do not have access to the high-dimensional state of the system, only a portion of it, represented in red in the input vector of the network. These values correspond to the position of the free surface of the fluid. Thus, the encoder must be substituted in step 3 by a GRU that takes the near history of the free surface to convert it into the reduced-order encoding of the system that will feed the thermodynamics-informed time integrator.

4.1 Model reduction based on autoencoders

In spite of the advances in terms of computational resources and calculation power, as well as capacity of storage, model order reduction is still a necessary tool to deal with the abundance of data and the physical complexity of certain phenomena. Training a complex database could truncate the convergence to an optimal result. Such is the case of the database available to build the model of the present work. In addition, operating on a low-dimensional manifold could also foster the robustness and stability of the proposed learning scheme so that changes in the input do not strongly condition the stability of the solution.

Currently, the development of these techniques is focused on capturing the important features of the non-linearities of these cases. Fluid dynamics are lead by strong non-linear structures hard to be learnt by machine learning methods. New approaches arise from the perspective of autoencoders [60] [61] as a preprocessing step in learning to deal with turbulence and instabilities.

Given a set of snapshots that live in a smooth finite-dimensional manifold $\mathcal{M} \in \mathbb{R}^D$, with $D = 13M$, as discussed in Eq. (3), we aim to find a projection to a manifold of latent variables $\mathcal{N} \in \mathbb{R}^d$ of much lower dimensionality, $d \ll D$. Autoencoders are an alternative to perform such reduction by finding patterns in the spatiotemporal structure of data. They are neural networks based on unsupervised learning. They consist of two parts, an encoder that maps data to an embedded space, and a decoder that reconstructs latent information to the original space. They set the target value of the decoder $\hat{\mathbf{z}}_t = \hat{\mathbf{z}}(t)$ to be equal to the input $\mathbf{z}_t = \mathbf{z}(t)$, and backpropagate the loss to enhance the reconstruction,

$$\text{Encoder } \phi : \mathcal{M} \subset \mathbb{R}^D \rightarrow \mathbb{R}^d \mathbf{z} \mapsto \mathbf{x},$$

$$\text{Decoder } \psi : \mathcal{N} \subset \mathbb{R}^d \rightarrow \mathbb{R}^D \mathbf{x} \mapsto \hat{\mathbf{z}}.$$

These schemes have shown good performance unveiling non-linear features to provide low and accurate representations of the information. In this work we have decided to use sparse autoencoders (SAE) so as to avoid as much as possible to figure out the dimensionality of the problem. This is accomplished automatically by the sparse autoencoder, by employing L1-norm penalization [62]. This can be interpreted, in the light of scientific machine learning, as a very practical form of imposing parsimony—in other words, Occam’s razor—to the learned model [8].

The backpropagated loss has two terms. With N_{snap} as the number of snapshots introduced in the algorithm, the first loss term $\mathcal{L}_{\text{mse}}^{\text{sae}}$ evaluates the reconstruction error between the ground truth and the result of the decoder,

$$\mathcal{L}_{\text{mse}}^{\text{sae}} = \frac{1}{N_{\text{snap}}} \sum_{i=1}^{N_{\text{snap}}} (\mathbf{z}_i - \hat{\mathbf{z}}_i)^2. \quad (1)$$

It is measured with the mean squared error (MSE) between the output and the input. Secondly, a regularizer term $\mathcal{L}_{\text{reg}}^{\text{sae}}$ is introduced to enforce the sparsity of the solution for the latent state snapshots \mathbf{x}_i ,

$$\mathcal{L}_{\text{reg}}^{\text{sae}} = \sum_{i=1}^{N_d} |\mathbf{x}_i|, \quad (2)$$

where N_d is the dimension of the latent vector of the autoencoder. This is fixed a priori as a big enough value, and the number of non-vanishing entries (i.e., the intrinsic dimensionality of data) will be determined without user intervention during the train period.

The regularization contribution is weighted with a coefficient $\lambda_{\text{reg}}^{\text{sae}}$ to control its influence in the training process,

$$\mathcal{L}^{\text{sae}} = \mathcal{L}_{\text{mse}}^{\text{sae}} + \lambda_{\text{reg}}^{\text{sae}} \mathcal{L}_{\text{reg}}^{\text{sae}}. \quad (3)$$

Although we have applied normalization over the dataset to perform learning, we decided to embed each group of state variables (position, velocity, internal energy, and stress tensor separated in normal $\boldsymbol{\sigma}$ and shear $\boldsymbol{\tau}$ components) separately to capture all the important features of each group of variables. In other words, we define five different autoencoders. The latent variables coming from each autoencoder together will form the complete latent space of the dynamics. This decision has been taken for optimization and accuracy reasons. The five encoders to be defined have the same structure. The encoder and decoder have the same architecture, but inverted. They have been defined as fully connected and non recursive layers that follow a feed-forward scheme.

4.2 Recurrent neural networks for state reconstruction

The latent space is built from pseudo-experimental data obtained from simulation, for which we have a full description of the different fluid states. Synthetic data includes internal variables important in our description, whereas they are

unmeasurable by ordinary means from camera inputs. We hypothesize with the fact that, although internal variables are not measurable, their influence can be unveiled from the dynamical evolution. As a result, we could analyze the features of the history of the dynamics where these variables will be reflected.

Self-supervised learning refers to a framework of techniques that aim to recover unknown information that we need in the description of a method. We propose an approach based on recurrent neural networks (RNNs), which are structures that take into consideration the history of data. They work over sequences to deal with time evolution instead of considering data simply as discrete and individual snapshots. RNNs are widely used, specially in the fields of natural language processing, speech recognition or economics. Vanilla RNN often encounter, however, vanishing and exploding gradient problems [63]. Gated Recurrent Units (GRU) [64] and Long Short-Term Memory (LSTM) units [65] are architectures capable of dealing with these problems. They include *gates* to keep important information in long or complex sequences while forgetting irrelevant features. GRUs have two main gates: an update gate, to update the hidden state, and a reset gate, which evaluates whether the previous cell state is relevant. In contrast with LSTMs, GRUs do not have a forget gate, which controls what is considered important to be remembered or to be rendered futile, and has less parameters. In spite of having a simpler structure, GRU's performance is similar to LSTM in certain tasks. In fact, GRUs have been proven to train faster and more efficiently with smaller datasets and shorter sequences [66].

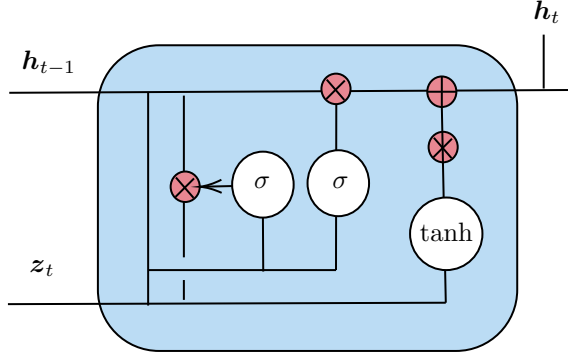


Figure 2: Representation of a GRU cell. The three main paths indicated represent the update and reset gates, the new memory cell, and their connection to update the new hidden state transmitted to the next later.

The basic idea behind the GRU architecture is to accumulate information from previous layers, see Fig. 2. The hidden state \mathbf{h}_t represents a kind of a summary of the features identified in previous sequences. $\mathbf{g}_t^{\text{update}}$ is the output of the update gate. This gate selects which information from the hidden state and the input sequence passes to the next step, modeled with a sigmoid activation function. As it models the past information that must be considered into the future, it resembles to the information with regard to the internal variables that will influence the reconstruction. In contrast, the reset gate \mathbf{r}_t reflects the past information that should be avoided. A new memory cell \mathbf{n}_t is defined with regard to the reset information to store only the relevant information from the past. The output is the final hidden state \mathbf{h}_t that accumulates the relevant information of past states and features learnt from the current input sequence:

$$\begin{aligned} \mathbf{g}_t^{\text{update}} &= \sigma(\mathbf{x}_t \mathbf{U}^z + \mathbf{h}_{t-1} \mathbf{W}^z), \\ \mathbf{r}_t &= \sigma(\mathbf{x}_t \mathbf{U}^r + \mathbf{h}_{t-1} \mathbf{W}^r), \\ \mathbf{n}_t &= \tanh(\mathbf{x}_t \mathbf{U}^h + (\mathbf{r}_t \mathbf{h}_{t-1}) \mathbf{W}^h), \\ \mathbf{h}_t &= (1 - \mathbf{g}_t^{\text{update}}) \mathbf{h}_{t-1} + \mathbf{g}_t^{\text{update}} \mathbf{n}_t. \end{aligned}$$

The input of the network consists of a sequence of measurements of the position of the free surface of the fluid. Since it is firstly trained with computational data, we select the particles of the discretization that belong to the free surface at each time step. The batch of sequences is introduced in the network to pass through GRU recurrent layers doing a projection *from-many-to-one*, i.e., introducing a sequence to obtain a single vector as output. The output vector of the GRU layers passes through a final forward fully connected layer with linear activation. The result of this process $\hat{\mathbf{x}}_t$ must match the latent state vector corresponding to the last snapshot \mathbf{x}_t of the given sequence. The loss $\mathcal{L}_{\text{mse}}^{\text{GRU}}$ evaluates the MSE between the predicted latent state and the ground truth,

$$\mathcal{L}_{\text{mse}}^{\text{GRU}} = \frac{1}{N_{\text{snap}}} \sum_{i=1}^{N_{\text{snap}}} (\mathbf{x}_i - \hat{\mathbf{x}}_i)^2. \quad (4)$$

4.3 Learning the dynamical evolution based on Structure Preserving Neural Networks

We have already mentioned the fact that one of our primary interests is to develop a technique that satisfies known basic principles of physics. Thus, the learned time integrator should respect first principles of physics so as to provide credible predictions of future events to help in the decision making process. By structure-preserving neural networks (SPNN) we refer to a class of techniques that are constructed so as to satisfy some a priori known properties of the problem such as equivariance [67] or energy conservation [53] [56]. In their most general form, they can be applied to conservative as well as dissipative problems, in which the principles of thermodynamics are satisfied by construction [48] [47]. In the case of SPNN we work from a thermodynamical perspective to drive learning through thermodynamically admissible scenarios that will ensure the consistency of the results. Therefore, we employ inductive biases that come from thermodynamic priors.

When the phenomenon at hand is dissipative, a particularly convenient formalism to describe its evolution in time is GENERIC. It presents a formulation to model the evolution of the vector of variables z from the analysis of the energy (Hamiltonian) potential in conjunction with a second (Massieu) potential that captures the dissipative nature of the dynamics. It is expressed in terms of Poisson and friction brackets, which can be reformulated as matrix operators, as

$$\frac{dz}{dt} = \mathbf{L}(z) \frac{\partial E(z)}{\partial z} + \mathbf{M}(z) \frac{\partial S(z)}{\partial z}. \quad (5)$$

The product of the gradient of energy and the symplectic matrix, $\mathbf{L}\nabla E$, models the conservative part of the time evolution, while the entropy gradient and the friction matrix $\mathbf{M}\nabla S$ capture the occurring dissipative effects beyond equilibrium. To discern which part of the evolution is governed by conservative phenomena and which one by dissipation, an additional condition must be imposed, the so-called degeneracy conditions,

$$\mathbf{L} \frac{\partial S}{\partial z} = \mathbf{0}, \quad \mathbf{M} \frac{\partial E}{\partial z} = \mathbf{0},$$

that state that energy has nothing to do with dissipation (it is conserved in closed systems) and entropy is not responsible of reversible phenomena.

In fact, these degeneracy conditions guarantee the conservation of energy,

$$\dot{E}(z) = \nabla E(z) \cdot \dot{z} = \nabla E(z) \cdot \mathbf{L}(z) \nabla E(z) + \nabla E(z) \cdot \mathbf{M} \nabla S(z) = 0,$$

and the production of entropy,

$$\dot{S}(z) = \nabla S(z) \cdot \dot{z} = \nabla S(z) \cdot \mathbf{L}(z) \nabla E(z) + \nabla S(z) \cdot \mathbf{M} \nabla S(z) \geq 0,$$

respectively.

These requirements are guaranteed if we choose \mathbf{L} and \mathbf{M} to be skew-symmetric and symmetric, positive semidefinite, respectively. For the sake of clarity, it is worth mentioning that GENERIC preserves these properties in the full-order as well as in the reduced-order manifold, enabling the learning of its structure in the latent space. In other words, it works equally well for z and x , provided that x represent well the dynamics.

We work on a discretized context of data samples, and learning is performed over a discrete expression of GENERIC. In this case, we consider a Forward Euler approximation of the time derivative that describes the dynamical evolution of the system. From this expression, the discrete degeneracy conditions to be imposed can be straightly derived:

$$\frac{x_{n+1} - x_n}{\Delta t} = \mathbf{L}(x_{n+1}) \mathbf{DE}(x_{n+1}) + \mathbf{M}(x_{n+1}) \mathbf{DS}(x_{n+1}), \quad (6)$$

where \mathbf{L} , \mathbf{M} , \mathbf{DE} and \mathbf{DS} represent the discretized versions of \mathbf{L} , \mathbf{M} , ∇E and ∇S , respectively, and the subscript n refers to time $t = n\Delta t$ and $n + 1$ indicates time $t + \Delta t$, respectively.

The SPNN follows a feed-forward flow which consists of a set of fully connected layers that learn the gradients of energy and entropy as well as the matrices \mathbf{L} and \mathbf{M} . The learning scheme enforces the skew-symmetry and symmetry of \mathbf{L} and \mathbf{M} respectively and the degeneracy conditions. Given pairs of consecutive snapshots, the neural network learns the integrator of the dynamical problem. The input is the state vector of latent variables at time t and $t + \Delta t$, x_n and x_{n+1} . The output coming from the net is a vector which contains the predicted \mathbf{L} , \mathbf{M} , and gradients of energy and entropy of the current state. During runtime, the time integration is consecutively performed with these operators.

The loss that carries the information to train and guide the SPNN is composed by two different terms. Firstly, the final output coming from the integration must match the ground truth. The accuracy is evaluated by measuring the mean squared error of these quantities,

$$\mathcal{L}_{\text{mse}}^{\text{SPNN}} = \frac{1}{N_{\text{snap}}} \sum_{i=1}^{N_{\text{snap}}} (x_i - \hat{x}_i)^2. \quad (7)$$

Secondly, training is also governed by the degeneracy conditions. They are taken into account as a loss coming from the sum of the squared values of both conditions,

$$\mathcal{L}_{\text{deg}}^{\text{SPNN}} = \frac{1}{N_{\text{snap}}} \sum_{i=1}^{N_{\text{snap}}} (\mathbf{L}_i \mathbf{D} \mathbf{S}_i)^2 + (\mathbf{M}_i \mathbf{D} \mathbf{E}_i)^2. \quad (8)$$

Finally, the MSE loss is weighted with the hyperparameter $\lambda_{\text{mse}}^{\text{SPNN}}$ to control its influence in the complete loss function of the network with regard to the problem,

$$\mathcal{L}^{\text{SPNN}} = \lambda_{\text{mse}}^{\text{SPNN}} \mathcal{L}_{\text{mse}}^{\text{SPNN}} + \mathcal{L}_{\text{deg}}^{\text{SPNN}}. \quad (9)$$

5 Training and validation

We train the learning process of sloshing dynamics from computational simulations. Each of the performed simulations are 2 seconds long, time at which the fluid reaches the equilibrium state. From them, we obtain snapshots which are equally spaced by time increments of 0.005 seconds. As a result, we have 1600 snapshots available for training. This dataset is split in two subsets, 80% for training and 20% for test. The same training subsets are employed for training and evaluation of the three networks.

Once the three nets are trained, we assemble the algorithm to feed the simulation loop with only a sequence of limited data. Instead of providing all the state variables obtained from the simulations, we pretend we have only measured the position at some points of the free surface. The sequence will be projected to the latent space, the SPNN will learn the dynamics, and the decoder will output results of the simulation augmenting the information originally given. The decoder provides the whole reconstruction of the fluid as well as the velocities, stresses and internal energy.

5.1 Hyperparameters and characteristics of each net

Each snapshot consists of a state vector of the position, velocity, internal energy and stresses (shear and normal) evaluated at each particle of the discretized fluid. The fluid is discretized in 2134 particles. Thus, the global dimensionality is 27742.

The SAE is subdivided in five different SAE, one for each subset of state variables. The nets have been initialized following the Kaiming method. In addition, we apply linear activations in the first and last layers, and ReLU for hidden layers. The optimizer chosen for these nets is Adam. A scheduler is programmed for updating the learning rate after 1000 and 3000 epochs.

We adapt the architectures according to the input dimension and their complexity or noisy nature of the values:

- Position: Input size is $D = 6402$ and output size $d = 20$. It is composed by $N_h = 2$ hidden layers of size 120.
- Velocity: Given the complexity of the velocity, we built a net of input size $D = 6402$, output size $d = 20$, $N_h = 4$ hidden layers, and hidden size 200.
- Internal energy: In the case of energy, input size is $D = 2134$, output size $d = 10$, and there are $N_h = 3$ hidden layers which consist of 40 neurons each.
- Normal stress: The normal stress tensor components are identical. Thus, the input shape of the net is $D = 2134$, the output shape is $d = 20$, and it is composed of $N_h = 3$ hidden layers of 200 neurons.
- Shear stress: This net had input size $D = 6402$, $N_h = 3$ hidden layers of 200 neurons, and output size $d = 20$.

The specific learning parameters such as learning rate (lr), weight decay (wd) and sparse weights (λ^{sae}) are established individually for each SAE. Table 1 shows the parameters defined for each net.

After 10000 epochs, SAEs converge to optimal results. Taking into account the sparsity imposed to improve the reduction, the final dimension of each net is $d_{\text{position}} = 3$, $d_{\text{velocity}} = 3$, $d_{\text{energy}} = 2$, $d_{\sigma} = 3$ and $d_{\tau} = 2$. Thus, the final shape of the reduced space is $d_{\text{latent space}} = 13$. The latents obtained are the output of the RNN, and the input of the SPNN. This substantial reduction will not only reduce computing time and storage, but also improve the convergence to a solution in subsequent trainings.

The recurrent neural network relates partial measurements of the fluid to the latent space that we have built. We consider that the only information accessible by ordinary means in real time is information related to the free surface of the fluid. Specifically, we pretend we can only measure the position at some points of the free surface.

Table 1: Training parameters for each SAE.

	lr	wd	$\lambda^{\text{saе}}$
Position	10^{-4}	10^{-6}	10^{-3}
Velocity	10^{-4}	10^{-5}	10^{-3}
Internal energy	10^{-4}	10^{-5}	10^{-4}
Normal stress	10^{-4}	10^{-5}	5×10^{-3}
Shear stress	10^{-3}	10^{-6}	5×10^{-3}

Table 2: Training and test loss of SAE after 10000 epochs

	Training Loss	Test Loss
Position	1.49×10^{-5}	1.60×10^{-5}
Velocity	4.1×10^{-4}	4.5×10^{-4}
Internal energy	4.72×10^{-5}	6.93×10^{-5}
Normal stress	5.11×10^{-4}	6.25×10^{-4}
Shear stress	7.98×10^{-5}	8.55×10^{-5}

We take each full-order snapshot of the database to find the particles that represent the free surface of the liquid. Those points do not necessarily follow a balanced distribution, i.e. they are not uniformly distributed in the free surface. We interpolate a uniform free surface with the information of the particles. This step facilitates comparison between sequences in future predictions. As a result, we have equally discretized free surfaces of 21 points, which results in a vector of size 42. In spite of reconstructing a 3D representation of fluids, we only consider a 2D data projection in the recurrent autoencoder. This projection represents the coordinates of the surface in the direction of the movement, and their vertical height due to the sloshing effect.

Once we have the information related to the free surface at each time step, we create the sequences. We consider sequences of 16 snapshots. This parameter has been chosen from analyzing training results. It is the minimum sequence size to guarantee that the features of the dynamics are correctly captured. With smaller sequences, the RNN does not learn good projections to the latent space. Since it is a short, although complex, sequence, GRU is optimal for this case.

Even though the time step of the data in our database is 0.005 seconds, the camera we work with streams depth measurements at a frequency of 60 Hz. Therefore, to assemble the sequences, we must choose snapshots equally spaced by approximately 0.015 seconds.

The input size of the net is batch size \times sequence length \times vector size. The net consists of three GRU hidden layers of 26 neurons, and there is a last feed forward fully connected layer to connect the last GRU layer to the latent space of size 13. This last layer has linear activation. The optimizer for training this net is Adam, and parameters are set to $lr = 10^{-3}$, $wd = 10^{-5}$. The learning rate is updated by a scheduler at 1000 and 3000 epochs.

We reach good results after 10000 epochs. Training loss is 1.19×10^{-3} , and test loss reaches a value of 2.3×10^{-3} .

The SPNN learns the integration scheme of the dynamics in the low manifold reached with the SAE. The input of the net are the latent variables, so the input size is 13. Providing that L and M are skew symmetric and symmetric, respectively, we only learn the upper elements of the main diagonal. Thus, instead of learning the full matrices of dimension $d \times d$, we learn $d \cdot (d - 1)/2$ elements for L and $d \cdot (d + 1)/2$ elements for M . Therefore, considering that the gradients have size d , the final output size is $d_{out} = d \cdot (d - 1)/2 + d \cdot (d + 1)/2 + d + d = 195$.

We have reduced the complexity of the dynamics thanks to the model order reduction applied. In spite of it, the dynamics and the latent evolution are still complicated for training. We require a structure of $N_h = 13$ hidden layers of size 195.

The SPNN has been also initialized following the Kaiming method. We have applied ReLU activations for hidden layers, and linear activations in the first and last layers. The initial parameters are set to $lr = 10^{-3}$, $wd = 10^{-5}$. The optimizer selected for training is also Adam, and the scheduler updates the learning rate after 1500, 2400, and 4000 epochs. The weight assigned to the MSE loss is $\lambda_{\text{mse}}^{\text{spnn}} = 10^3$, to give more importance to the reconstruction.

We train the SPNN for 5000 epochs. At that point the training and test losses are 3.2×10^{-3} and 1.42×10^{-2} , respectively.

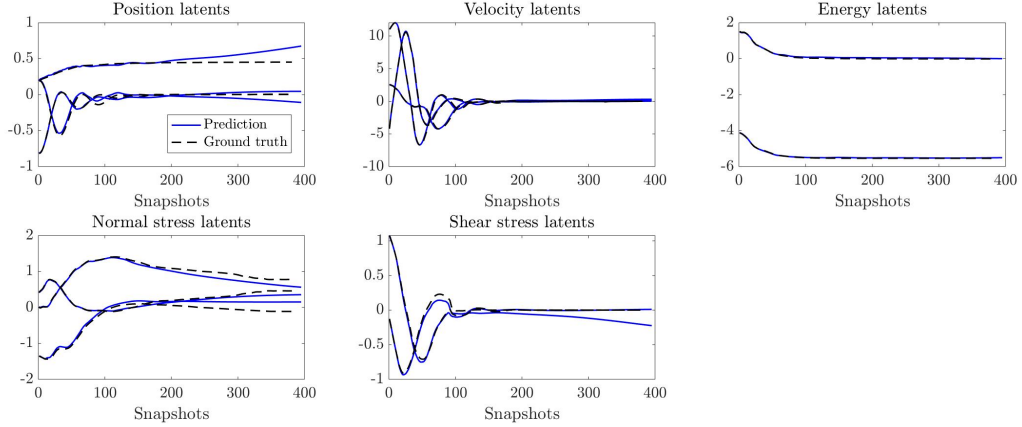


Figure 3: Simulation results. Learning of the dynamics in the latent manifold. Dashed lines represent the time evolution of the latents that aimed to be emulated. Lines in blue represent the result of the SPNN in the latent manifold.

Table 3: Computational learning error

	Latents learning	Real system learning
Position	3.1×10^{-3}	1.25×10^{-4}
Velocity	1.91×10^{-2}	5.037×10^{-4}
Internal energy	1.2×10^{-3}	4.64×10^{-5}
Normal stress	1.22×10^{-2}	3.9×10^{-3}
Shear stress	4.7×10^{-3}	3.87×10^{-4}

5.2 Initial validation

The performance of the method is tested with an input sequence extracted from the simulation of initial velocity 0.2 m/s. Given this sequence, the information is mapped to the latent state. Once we obtain the latent variables corresponding to that sequence, the SPNN integrates the dynamics until the fluid reaches the steady state. We could provide information of sequences at each time step, but data acquisition is not always accessible in real scenarios (occlusion, connection problems, ...) In those cases, the simulation should continue until new information is provided. To this end, we test the ability of the method to continue integrating and the stability of the simulation and results by providing it with only one snapshot as initial condition.

Figure 3 represents a plot of the integration results in the reduced-order space. The initial state has been projected to the latent manifold to follow the evolution of its behavior. The dashed lines represent the trajectory that should be reproduced by the SPNN net, and the blue lines show the learnt behavior for the given sequence. Also, Fig. 4 shows the comparison between the ground truth and the projection of the integrated latent variables at three time steps once the latents have been reprojected to the physical, high-dimensional manifold. The error breakdown obtained in both latent and real spaces for each state variable is shown in Table 3. After analyzing the results obtained in the computational phase, we decide to test the loop in a real scenario for reconstruction of real fluids.

6 Tests with real-world data

Once the proposed strategy has been tested on computational data, it is extended to real-world problems. An RGBD camera is used to track the free surface of the fluid. This information is converted into sequences to predict the next state of its time evolution. Finally, we have not only a reconstruction, but an augmented representation of the fluid providing velocity, internal energy and stress fields.



Figure 4: Comparison of the reconstruction of the integration provided by the SPNN (right) with the ground truth (left). The selected snapshots correspond to peaks of the sloshing dynamics of glycerine. Specifically we present the comparison for snapshots 1, 33 and 64 of the collection.

6.1 Data acquisition review

Firstly, we need to detect the free surface of the fluid and perform measurements to feed the algorithm with real data. We make use of a stereo camera for this purpose, although many of the presented results could equally be obtained with a standard camera. The model of our stereo camera is RealSense D415 (<https://www.intelrealsense.com/depth-camera-d415/>). This model of stereo camera provides both intrinsic and extrinsic parameters as well as depth measurements. Thus, the projection of the 2D to the 3D, and viceversa, is straight forward. The free surface is detected with regard to the pixel coordinates of each point u, v . The software provides the intrinsic parameters f_x, f_y, c_x, c_y, s , which are the focal length, the optical center coordinates and the skew coefficient respectively. In addition to the intrinsic parameters K , we can also estimate (by means of Simultaneous Localization and Mapping techniques [68]), the rotation \mathbf{R} and translation \mathbf{t} components to complete the projection to the real world coordinates X, Y, Z of the point \mathbf{p}_w ,

$$s \begin{bmatrix} u \\ v \\ 1 \end{bmatrix} = \begin{bmatrix} f_x & 0 & c_x \\ 0 & f_y & c_y \\ 0 & 0 & 1 \end{bmatrix} \begin{bmatrix} r_{11} & r_{12} & r_{13} & t_1 \\ r_{21} & r_{22} & r_{23} & t_2 \\ r_{31} & r_{32} & r_{33} & t_3 \end{bmatrix} \begin{bmatrix} X \\ Y \\ Z \\ 1 \end{bmatrix},$$

$$\tilde{\mathbf{x}}_s = \mathbf{K}[\mathbf{R}|\mathbf{t}]\mathbf{p}_w.$$

A sketch of the camera system is depicted in Fig. 5.

It is worth mentioning that the original frame does not provide good enough depth measurements. It reports holes where the algorithm did not successfully measure the depth of the pixels. Measurements related to transparent objects are often invalid or noisy since their surfaces are not Lambertian, which is the main assumption of the measurement algorithm incorporated in the stereo camera. In other words, instead of reflecting light evenly in all directions they also refract light, resulting in unmeasurable conditions for the technique defined. Our approach consists in applying some filters to enhance the depth streaming. Firstly, we apply a decimation filter to reduce the complexity of the measurements to foster stability. Then, the frame is mapped to a disparity map where the spatial filter, to preserve the edges, and the temporal filter, to promote data persistency, are applied. This result is projected back to the depth map where the

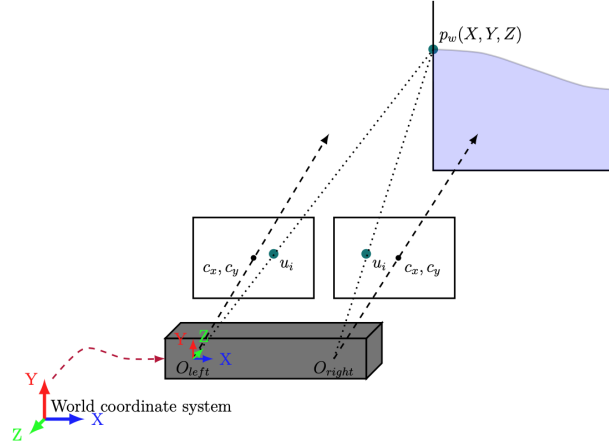


Figure 5: Representation of the data acquisition system. The free surface is the tracked element of the algorithm to perform learning and the simulation of the dynamics.

hole-filling filter is finally applied. The filtered depth map outputs a full depth field from which we can evaluate the position of the glass and the free surface (see Fig. 6).

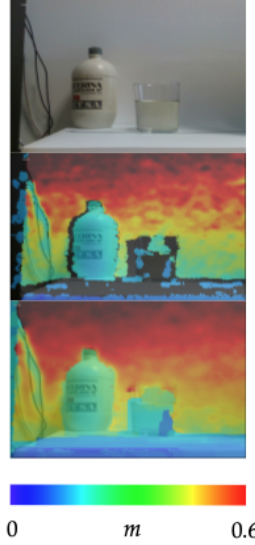


Figure 6: Color and depth stream before (up) and after (down) applying the required filters to reconstruct the depth map of the streaming.

We binarize the color frame, also streamed by the camera, to convert the image into a black and white picture. The free surface appears as a gradient in the black and white image, see Fig. 7. Since we value the speed in the data streaming, we define an area for performing these analysis instead of forcing the recognition across the full image. The points of the free surface are detected, tracked, projected from frame coordinates to 3D, and stored.

6.2 Reconstruction and integration from video streaming

We assemble the sequences with the data obtained from the data acquisition step. These sequences feed the algorithm trained with computational data. The RNN projects the sequences to the latent space, the SPNN integrates the dynamics, and the decoder projects back not only the next state of the free surface, but also the position of the whole set of particles as well the velocity, internal energy, σ and τ . Therefore, we reconstruct the complete state of the fluid at the next time



Figure 7: Representation of the color frame and its conversion to a binarized image to seek the free surface. The area defined for searching is represented in the color frame as well as the points of the free surface detected in the black and white image.

step only from the free surface. Video streams consist of 800 frames, which represent a recording of 12 seconds, with which we obtain the next results.

Figure 9 shows the results of the algorithm compared to the real video streaming. We perform the reconstruction and integration over the whole sequence, i.e. no cuts were applied to the streaming and the method is applied continuously. All the results outputted come from the integration. We perform the three steps (RNN projection, integration, and decoding) of the full video in 3.42 seconds on an ordinary laptop (Macbook Pro 2013-3 GHz Intel Core i7), achieving (much more than) the real-time performance proposed. Some snapshots of a sloshing phenomenon were selected and plotted in the first row of Fig. 8. The snapshots shown represent the peaks, which are the most critical states in manipulation, and some intermediate states between the peaks. The following pictures correspond to the augmented information obtained in this method, which has been possible due to the physics-aware simulation framework.

All results of the integration are stable, realistic, and close to the real result. We analyze objectively the results by evaluating the root mean squared error (RMSE) between the real \mathbf{y} and the predicted $\hat{\mathbf{y}}$ free surfaces in n snapshots of the video streaming,

$$\text{RMSE} = \sqrt{\frac{1}{n} \sum_{t=1}^n (\hat{\mathbf{y}}_i - \mathbf{y}_i)^2}.$$

The evolution of the error along the video is represented in Fig. 10. The error remains under 5 mm in the whole sequence of the length of the video, and stays lower than 3 mm in the vast majority of it.

Fig. 11 showcases finally the compliance of the principles of the thermodynamics in the predictions. The time derivative of energy makes little oscillations due to the numerical approximation around 0, which means that we ensure the conservation of energy. In addition, the time derivative of entropy remains always positive, fulfilling its production.

7 Conclusions and future work

In this work we have presented an approach for the physical perception of sloshing phenomena. It is based upon physics-informed learned simulators connected to the real world by means of commodity RGBD cameras. The algorithm has been trained with computational data to build a physically sound reduced-order manifold to learn the evolution of the dynamics dictated by the General Equation for the Non-Equilibrium Reversible-Irreversible Coupling (GENERIC). This thermodynamic framework ensures the physical consistency, accuracy and realism of the results to promote informed decision making.

Provided the physics-aware approach for learning, only four simulations per fluid were needed to perform a training that accurately mimics computational and real behaviors. This approach to work with limited data has been completed with the development of a self-supervised technique to recover information of the dynamics that is unmeasurable by ordinary means. In spite of the existence of sensors and advanced tools, such as PIV cameras, for evaluating data that cannot be extracted from simple video streamings, we are still unable to evaluate important information for a complete physical description. The suggested methodology fills in the gaps of information for recovery and projection of future dynamical states.

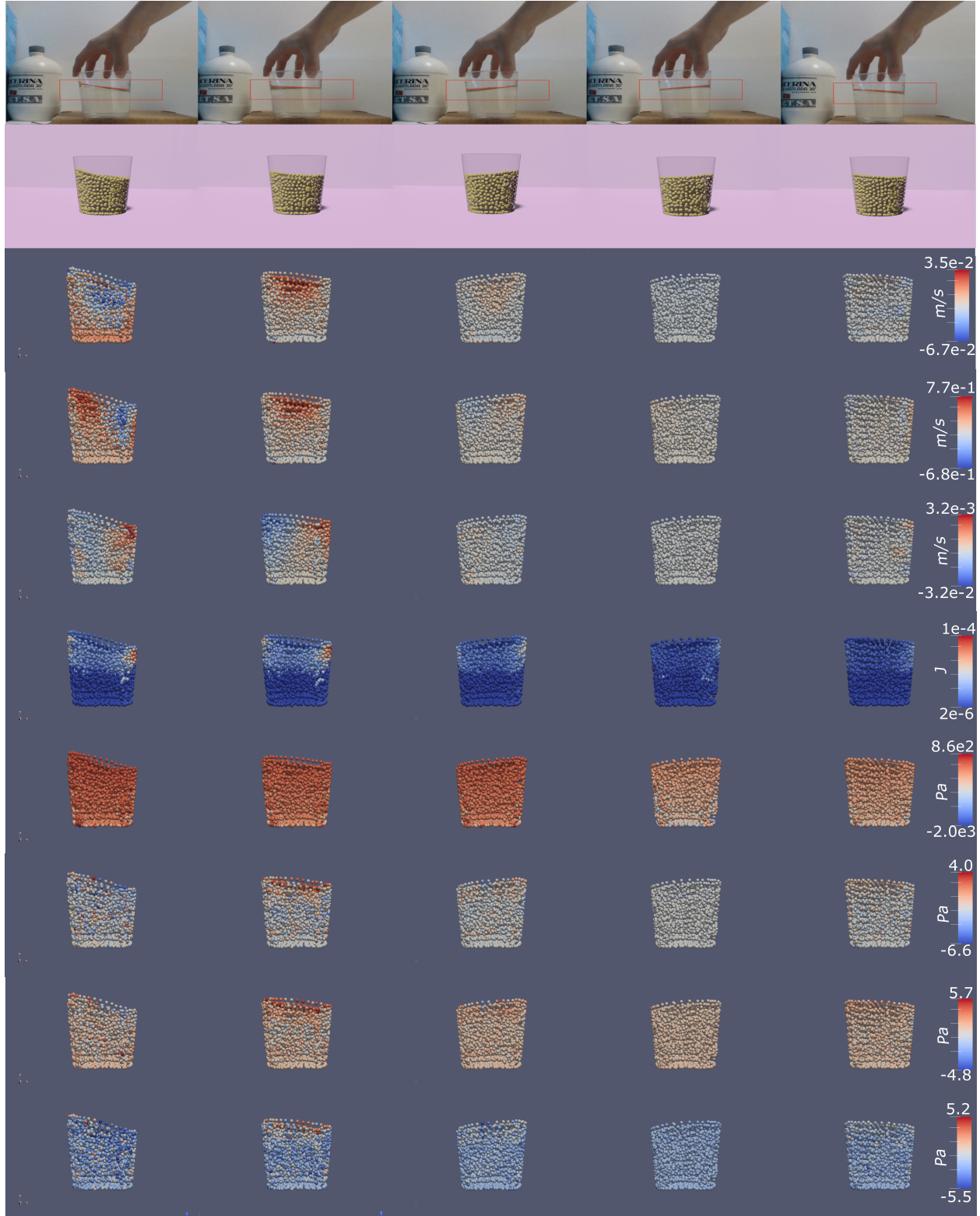


Figure 8: Results of the perception of a case of a 12 seconds video of a glass of glycerine. Eight snapshots of the sloshing sequence were selected for comparison. The selected snapshots have index 560, 565, 568, 572, 578 from left to right. The second row corresponds to the fluid reconstruction and prediction provided the previous snapshot. From row three to ten we show the additional information obtained from the reconstruction and simulation (velocity, energy and stress fields, respectively).

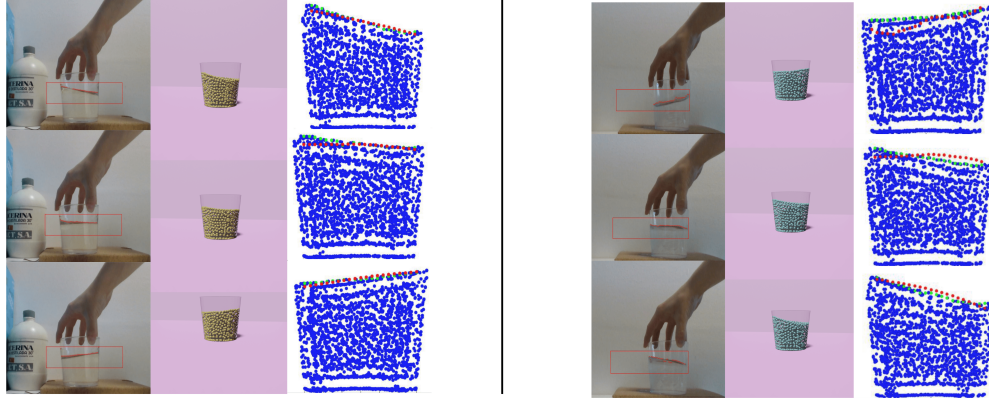


Figure 9: Detail of the comparison of glycerine (left) and water (right) with the prediction. The third column of both liquids compares the predicted fluid volume (in blue), the free surface of the liquid volume (green) and the target free surface (in red).

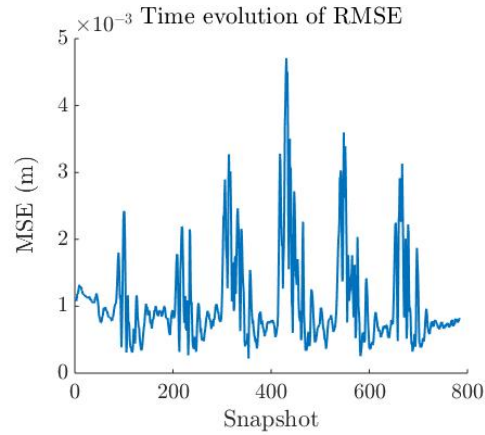


Figure 10: Evolution of the mean squared error during the perception process of sloshing in a glass of glycerine.

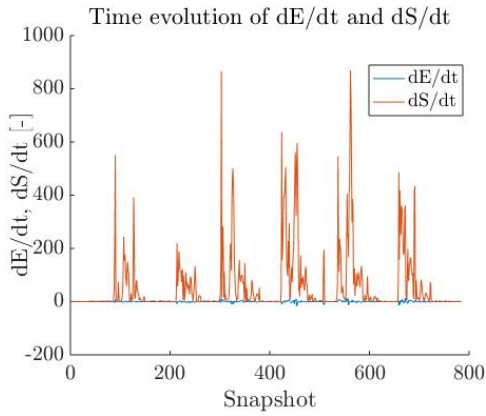


Figure 11: Time derivatives of energy and Entropy along the video. The time derivative of Energy oscillates around zero, ensuring energy conservation. Entropy production is also ensured since the time derivative is always positive.

Since the main purpose of the approach is to connect real-world systems with AI-guided simulators, we test the implementation of the integration scheme with a coupled data-acquisition system. The free surface is tracked by these means, and the information obtained is used for fluid prediction. Notably, real time is successfully achieved due to the

reduction obtained through the application of autoencoders: 12 seconds of real-world time are analyzed in slightly more than 3 seconds, thus allowing for the introduction of decision making or control algorithms in the loop. In addition, information is provided to the user by using augmented reality, i.e., by outputting the reconstructed fluid volume and a set of variables that may be important for decision making on top of the video stream.

Nonetheless, physics perception must achieve generality. It is unmanageable to train a model for each casuistic. Consequently, transfer learning must be extended to world and scene reasoning. Starting from a model such the one proposed, incremental learning could set the base to extend learning and build hybrid twins which learn the evolving scenario that a machine may have to control.

Acknowledgment

The work presented has been partially supported by the Spanish Ministry of Economy and Competitiveness through Grant number PID2020-113463RB-C31 and by the Regional Government of Aragon and the European Social Fund, research group T88. The authors also thank the support of ESI Group through the project UZ-2019-0060.

References

- [1] C. K. Liu and D. Negrut, “The role of physics-based simulators in robotics,” *Annual Review of Control, Robotics, and Autonomous Systems*, vol. 4, 2020.
- [2] C. J. Bates, I. Yildirim, J. B. Tenenbaum, and P. Battaglia, “Modeling human intuitions about liquid flow with particle-based simulation,” *PLoS computational biology*, vol. 15, no. 7, p. e1007210, 2019.
- [3] P. W. Battaglia, J. B. Hamrick, and J. B. Tenenbaum, “Simulation as an engine of physical scene understanding,” *Proceedings of the National Academy of Sciences*, vol. 110, no. 45, pp. 18 327–18 332, 2013.
- [4] C. Schenck and D. Fox, “Spnets: Differentiable fluid dynamics for deep neural networks,” in *Conference on Robot Learning*. PMLR, 2018, pp. 317–335.
- [5] L. Li, S. Hoyer, R. Pederson, R. Sun, E. D. Cubuk, P. Riley, K. Burke *et al.*, “Kohn-sham equations as regularizer: Building prior knowledge into machine-learned physics,” *Physical review letters*, vol. 126, no. 3, p. 036401, 2021.
- [6] M. Raissi, P. Perdikaris, and G. E. Karniadakis, “Physics informed deep learning (part i): Data-driven solutions of nonlinear partial differential equations,” *arXiv preprint arXiv:1711.10561*, 2017.
- [7] L. Yang, X. Meng, and G. E. Karniadakis, “B-pinn: Bayesian physics-informed neural networks for forward and inverse pde problems with noisy data,” *Journal of Computational Physics*, vol. 425, p. 109913, 2021.
- [8] Z. Liu and M. Tegmark, “AI Poincaré: Machine Learning Conservation Laws from Trajectories,” *arXiv preprint arXiv:2011.04698*, 2020.
- [9] K. L. Course, T. W. Evans, and P. B. Nair, “Weak form generalized hamiltonian learning,” *arXiv preprint arXiv:2104.05096*, 2021.
- [10] A. Sancarlos, M. Cameron, A. Abel, E. Cueto, J.-L. Duval, and F. Chinesta, “From rom of electrochemistry to ai-based battery digital and hybrid twin,” *Archives of Computational Methods in Engineering*, vol. 28, no. 3, pp. 979–1015, 2021.
- [11] B. Moya, I. Alfaro, D. Gonzalez, F. Chinesta, and E. Cueto, “Physically sound, self-learning digital twins for sloshing fluids,” *PLoS One*, vol. 15, no. 6, p. e0234569, 2020.
- [12] M. Grmela and H. C. Öttinger, “Dynamics and thermodynamics of complex fluids. i. development of a general formalism,” *Physical Review E*, vol. 56, no. 6, p. 6620, 1997.
- [13] Z. Lan, M. Chen, S. Goodman, K. Gimpel, P. Sharma, and R. Soricut, “Albert: A lite bert for self-supervised learning of language representations,” *arXiv preprint arXiv:1909.11942*, 2019.
- [14] M. Lewis, Y. Liu, N. Goyal, M. Ghazvininejad, A. Mohamed, O. Levy, V. Stoyanov, and L. Zettlemoyer, “Bart: Denoising sequence-to-sequence pre-training for natural language generation, translation, and comprehension,” *arXiv preprint arXiv:1910.13461*, 2019.
- [15] L. Jing and Y. Tian, “Self-supervised visual feature learning with deep neural networks: A survey,” *IEEE Transactions on Pattern Analysis and Machine Intelligence*, 2020.
- [16] P. Goyal, M. Caron, B. Lefauveaux, M. Xu, P. Wang, V. Pai, M. Singh, V. Liptchinsky, I. Misra, A. Joulin *et al.*, “Self-supervised pretraining of visual features in the wild,” *arXiv preprint arXiv:2103.01988*, 2021.

- [17] K. Wang, L. Lin, C. Jiang, C. Qian, and P. Wei, “3d human pose machines with self-supervised learning,” *IEEE transactions on pattern analysis and machine intelligence*, vol. 42, no. 5, pp. 1069–1082, 2019.
- [18] A. Tonioni, M. Poggi, S. Mattoccia, and L. Di Stefano, “Unsupervised domain adaptation for depth prediction from images,” *IEEE transactions on pattern analysis and machine intelligence*, vol. 42, no. 10, pp. 2396–2409, 2019.
- [19] C. Doersch, A. Gupta, and A. A. Efros, “Unsupervised visual representation learning by context prediction,” in *Proceedings of the IEEE international conference on computer vision*, 2015, pp. 1422–1430.
- [20] R. Zhang, P. Isola, and A. A. Efros, “Colorful image colorization,” in *European conference on computer vision*. Springer, 2016, pp. 649–666.
- [21] S. Gidaris, P. Singh, and N. Komodakis, “Unsupervised representation learning by predicting image rotations,” *arXiv preprint arXiv:1803.07728*, 2018.
- [22] D. Pathak, P. Krahenbuhl, J. Donahue, T. Darrell, and A. A. Efros, “Context encoders: Feature learning by inpainting,” in *Proceedings of the IEEE conference on computer vision and pattern recognition*, 2016, pp. 2536–2544.
- [23] T. Chen, S. Kornblith, M. Norouzi, and G. Hinton, “A simple framework for contrastive learning of visual representations,” in *International conference on machine learning*. PMLR, 2020, pp. 1597–1607.
- [24] I. Misra and L. v. d. Maaten, “Self-supervised learning of pretext-invariant representations,” in *Proceedings of the IEEE/CVF Conference on Computer Vision and Pattern Recognition*, 2020, pp. 6707–6717.
- [25] A. Nair, D. Chen, P. Agrawal, P. Isola, P. Abbeel, J. Malik, and S. Levine, “Combining self-supervised learning and imitation for vision-based rope manipulation,” in *2017 IEEE international conference on robotics and automation (ICRA)*. IEEE, 2017, pp. 2146–2153.
- [26] M. Nava, A. Paolillo, J. Guzzi, L. M. Gambardella, and A. Giusti, “Uncertainty-aware self-supervised learning of spatial perception tasks,” *arXiv preprint arXiv:2103.12007*, 2021.
- [27] M. Yan, Y. Zhu, N. Jin, and J. Bohg, “Self-supervised learning of state estimation for manipulating deformable linear objects,” *IEEE robotics and automation letters*, vol. 5, no. 2, pp. 2372–2379, 2020.
- [28] S. L. Brunton and B. R. Noack, “Closed-loop turbulence control: Progress and challenges,” *Applied Mechanics Reviews*, vol. 67, no. 5, 2015.
- [29] J. L. Callaham, K. Maeda, and S. L. Brunton, “Robust flow reconstruction from limited measurements via sparse representation,” *Physical Review Fluids*, vol. 4, no. 10, p. 103907, 2019.
- [30] L. Sun and J.-X. Wang, “Physics-constrained bayesian neural network for fluid flow reconstruction with sparse and noisy data,” *Theoretical and Applied Mechanics Letters*, vol. 10, no. 3, pp. 161–169, 2020.
- [31] N. B. Erichson, L. Mathelin, Z. Yao, S. L. Brunton, M. W. Mahoney, and J. N. Kutz, “Shallow neural networks for fluid flow reconstruction with limited sensors,” *Proceedings of the Royal Society A*, vol. 476, no. 2238, p. 20200097, 2020.
- [32] J. Yu and J. S. Hesthaven, “Flowfield reconstruction method using artificial neural network,” *Aiaa Journal*, vol. 57, no. 2, pp. 482–498, 2019.
- [33] K. O. Lye, S. Mishra, and D. Ray, “Deep learning observables in computational fluid dynamics,” *Journal of Computational Physics*, vol. 410, p. 109339, 2020.
- [34] Y. LeCun, Y. Bengio, and G. Hinton, “Deep learning,” *nature*, vol. 521, no. 7553, pp. 436–444, 2015.
- [35] P. W. Battaglia, J. B. Hamrick, V. Bapst, A. Sanchez-Gonzalez, V. Zambaldi, M. Malinowski, A. Tacchetti, D. Raposo, A. Santoro, R. Faulkner *et al.*, “Relational inductive biases, deep learning, and graph networks,” *arXiv preprint arXiv:1806.01261*, 2018.
- [36] A. K. Maier, C. Syben, B. Stimpel, T. Würfl, M. Hoffmann, F. Schebesch, W. Fu, L. Mill, L. Kling, and S. Christiansen, “Learning with known operators reduces maximum error bounds,” *Nature Machine Intelligence*, vol. 1, no. 8, pp. 373–380, 2019. [Online]. Available: <https://doi.org/10.1038/s42256-019-0077-5>
- [37] B. Lusch, J. N. Kutz, and S. L. Brunton, “Deep learning for universal linear embeddings of nonlinear dynamics,” *Nature communications*, vol. 9, no. 1, pp. 1–10, 2018.
- [38] J. Ayensa-Jiménez, M. H. Doweidar, J. A. Sanz-Herrera, and M. Doblaré, “Prediction and identification of physical systems by means of physically-guided neural networks with meaningful internal layers,” *Computer Methods in Applied Mechanics and Engineering*, vol. 381, p. 113816, 2021.
- [39] P. Jin, Z. Zhang, I. G. Kevrekidis, and G. E. Karniadakis, “Learning poisson systems and trajectories of autonomous systems via poisson neural networks,” *arXiv preprint arXiv:2012.03133*, 2020.

- [40] J. S. Hesthaven, C. Pagliantini, and N. Ripamonti, “Rank-adaptive structure-preserving reduced basis methods for hamiltonian systems,” *arXiv preprint arXiv:2007.13153*, 2020.
- [41] H. Yu, X. Tian, Q. Li *et al.*, “Onsagernet: Learning stable and interpretable dynamics using a generalized onsager principle,” *arXiv preprint arXiv:2009.02327*, 2020.
- [42] R. Ibañez, D. Borzacchiello, J. V. Aguado, E. Abisset-Chavanne, E. Cueto, P. Ladeveze, and F. Chinesta, “Data-driven non-linear elasticity: constitutive manifold construction and problem discretization,” *Computational Mechanics*, vol. 60, no. 5, pp. 813–826, 2017.
- [43] D. González, F. Chinesta, and E. Cueto, “Thermodynamically consistent data-driven computational mechanics,” *Continuum Mechanics and Thermodynamics*, vol. 31, no. 1, pp. 239–253, 2019.
- [44] ———, “Learning non-markovian physics from data,” *Journal of Computational Physics*, vol. 428, p. 109982, 2021.
- [45] C. Ghanatos, I. Alfaro, D. González, F. Chinesta, and E. Cueto, “Data-driven generic modeling of poroviscoelastic materials,” *Entropy*, vol. 21, no. 12, p. 1165, 2019.
- [46] B. Moya, D. González, I. Alfaro, F. Chinesta, and E. Cueto, “Learning slosh dynamics by means of data,” *Computational Mechanics*, vol. 64, no. 2, pp. 511–523, 2019.
- [47] Q. Hernandez, A. Badías, D. González, F. Chinesta, and E. Cueto, “Deep learning of thermodynamics-aware reduced-order models from data,” *Computer Methods in Applied Mechanics and Engineering*, vol. 379, p. 113763, 2021.
- [48] Q. Hernandez, A. Badias, D. González, F. Chinesta, and E. Cueto, “Structure-preserving neural networks,” *Journal of Computational Physics*, vol. 426, p. 109950, 2021.
- [49] A. Sanchez-Gonzalez, J. Godwin, T. Pfaff, R. Ying, J. Leskovec, and P. Battaglia, “Learning to simulate complex physics with graph networks,” in *International Conference on Machine Learning*. PMLR, 2020, pp. 8459–8468.
- [50] Y. Li, T. Lin, K. Yi, D. Bear, D. Yamins, J. Wu, J. Tenenbaum, and A. Torralba, “Visual grounding of learned physical models,” in *International Conference on Machine Learning*. PMLR, 2020, pp. 5927–5936.
- [51] J. Wu, I. Yildirim, J. J. Lim, B. Freeman, and J. Tenenbaum, “Galileo: Perceiving physical object properties by integrating a physics engine with deep learning,” *Advances in neural information processing systems*, vol. 28, pp. 127–135, 2015.
- [52] T. Bertalan, F. Dietrich, I. Mezić, and I. G. Kevrekidis, “On learning hamiltonian systems from data,” *Chaos: An Interdisciplinary Journal of Nonlinear Science*, vol. 29, no. 12, p. 121107, 2019.
- [53] S. Greydanus, M. Dzamba, and J. Yosinski, “Hamiltonian neural networks,” in *Advances in Neural Information Processing Systems*, 2019, pp. 15 379–15 389.
- [54] P. Jin, A. Zhu, G. E. Karniadakis, and Y. Tang, “Symplectic networks: Intrinsic structure-preserving networks for identifying hamiltonian systems,” *arXiv preprint arXiv:2001.03750*, 2020.
- [55] P. Toth, D. J. Rezende, A. Jaegle, S. Racanière, A. Botev, and I. Higgins, “Hamiltonian generative networks,” *arXiv preprint arXiv:1909.13789*, 2019.
- [56] Y. D. Zhong, B. Dey, and A. Chakraborty, “Symplectic ode-net: Learning hamiltonian dynamics with control,” *arXiv preprint arXiv:1909.12077*, 2019.
- [57] P. Español, *Statistical Mechanics of Coarse-Graining*. Berlin, Heidelberg: Springer Berlin Heidelberg, 2004, pp. 69–115. [Online]. Available: http://dx.doi.org/10.1007/978-3-540-39895-0_3
- [58] P. Espanol, M. Serrano, and H. C. Öttinger, “Thermodynamically admissible form for discrete hydrodynamics,” *Physical review letters*, vol. 83, no. 22, p. 4542, 1999.
- [59] J. J. Monaghan, “Smoothed particle hydrodynamics,” *Annual review of astronomy and astrophysics*, vol. 30, no. 1, pp. 543–574, 1992.
- [60] K. Taira, M. S. Hemati, S. L. Brunton, Y. Sun, K. Duraisamy, S. Bagheri, S. T. Dawson, and C.-A. Yeh, “Modal analysis of fluid flows: Applications and outlook,” *AIAA journal*, vol. 58, no. 3, pp. 998–1022, 2020.
- [61] N. B. Erichson, M. Muehlebach, and M. W. Mahoney, “Physics-informed autoencoders for lyapunov-stable fluid flow prediction,” *arXiv preprint arXiv:1905.10866*, 2019.
- [62] A. Ng *et al.*, “Sparse autoencoder,” *CS294A Lecture notes*, vol. 72, no. 2011, pp. 1–19, 2011.
- [63] R. Pascanu, T. Mikolov, and Y. Bengio, “On the difficulty of training recurrent neural networks,” in *International conference on machine learning*. PMLR, 2013, pp. 1310–1318.

- [64] K. Cho, B. Van Merriënboer, C. Gulcehre, D. Bahdanau, F. Bougares, H. Schwenk, and Y. Bengio, “Learning phrase representations using rnn encoder-decoder for statistical machine translation,” *arXiv preprint arXiv:1406.1078*, 2014.
- [65] S. Hochreiter and J. Schmidhuber, “Long short-term memory,” *Neural computation*, vol. 9, no. 8, pp. 1735–1780, 1997.
- [66] J. Chung, C. Gulcehre, K. Cho, and Y. Bengio, “Empirical evaluation of gated recurrent neural networks on sequence modeling,” *arXiv preprint arXiv:1412.3555*, 2014.
- [67] E. Celledoni, M. J. Ehrhardt, C. Etmann, R. I. McLachlan, B. Owren, C.-B. Schönlieb, and F. Sherry, “Structure preserving deep learning,” *arXiv preprint arXiv:2006.03364*, 2020.
- [68] R. Mur-Artal and J. D. Tardós, “Orb-slam2: An open-source slam system for monocular, stereo, and rgbd cameras,” *IEEE Transactions on Robotics*, vol. 33, no. 5, pp. 1255–1262, 2017.